PHYSICAL REVIEW E **71**, 056307 (2005)

Influence of excitation wave forms and frequencies on the fundamental time symmetry of the system dynamics, studied in nematic electroconvection

Thomas John, Jana Heuer, and Ralf Stannarius
Institut für Experimentelle Physik, Fakultät für Naturwissenschaften, Universität Magdeburg, Universitätsplatz 2, D-39106 Magdeburg, Germany

(Received 2 September 2004; published 27 May 2005)

The dynamics of periodically driven nematic electroconvection, a classical dissipative pattern forming system, is studied experimentally and theoretically. We demonstrate that for certain excitation wave forms, the system's dynamic response can be periodic with the excitation or subharmonic, depending on the periodicity of the excitation as control parameter, while for some classes of wave forms, a subharmonic response seems to be principally excluded. In particular, we describe influences of frequency and time symmetry of triangular excitation wave forms. Two intrinsically different routes for the transition to subharmonic dynamics are observed. The time characteristics of the system variables are determined by numerical solution of appropriate model equations and a Floquet analysis. Experimental data are compared to calculations of the model system of two coupled linear differential equations. Results of experiment and model are in excellent agreement.

DOI: 10.1103/PhysRevE.71.056307 PACS number(s): 47.20.−k, 05.45.−a, 61.30.−v, 47.54.+r

I. INTRODUCTION

Electrohydrodynamic convection (EHC) represents a well known and extensively investigated system for dissipative pattern formation. After the first experimental description (independently by Williams [1] and Kapustin [2]), the mechanism of the instability was revealed by Carr [3] and Helfrich [4]. There has been a rapid progress in the further development of the theory [5–12]. Still today, EHC represents an attractive research field: Focus of recent experimental and theoretical studies has been laid, e.g., on EHC in nonconventional materials [13], defects and localized states [14–18], spatiotemporal chaos [19,20], patterns in homeotropic geometry [21], or systems with low dimensionality [22,23]. The dynamics of the system variables in EHC patterns has been studied in particular in Refs. [5,6,24–27].

The two coupled dynamic variables that characterize the electroconvection patterns in a sandwich cell are the periodic director deflection in the cell and the charge density modulation. The director deflection is directly connected with the velocity of the convective flow in the cell. Figure 1 gives a schematic view of the cell geometry and the structure of the convection pattern.

Nematic electroconvection is conventionally studied under ac excitation. The control parameters of the experiment are amplitudes, frequencies, and wave forms of the applied voltage. These parameters are conveniently accessible in the laboratory, and even complex wave forms may be composed with commercial synthesizers. This makes the nematic EHC experiment particularly suitable for the study of the influence of excitation wave forms on pattern dynamics.

It is well known in spatially extended pattern forming dynamic systems that breaking of the time symmetry of the excitation, like the temporal modulation of the controll parameters, can influence the appearance of the patterns qualitatively. For example, in Rayleigh-Benard convection a temporally modulated control parameter can lead to the stabilization of hexagonal patterns against parallel rolls [28], and to a coexistence of rolls and hexagons. In particular, systems that undergo a Hopf bifurcation can be sensitive to broken time translational symmetry. Stimulated by theoretical analysis [29], the temporal modulation of control parameters has been used in EHC for the controlled conversion between traveling convection roll patterns (traveling waves) and standing waves [30]. We note, however, that the time symmetries discussed in the present paper have only a very indirect relation, if any, to the above cited studies of temporal modulations of the control parameter. In order to derive the wavelengths and dynamics of our convection patterns at onset in the different dynamic regimes, we do not need to employ amplitude equations, but rather perform a simple linear stability analysis.

From a mathematical point of view, a particularly interesting aspect is that a simple system of two coupled ordinary linear differential equations (ODE's) can be used to construct the pattern stability diagrams and the pattern dynamics at onset. The structure of the dynamic equations is such that in the classical experiment [electric field E with the period T and time symmetry $E(t)=-E(t+T/2)$], either the electric charge distribution or the director field changes its sign in each half period of the excitation. In the conduction regime,

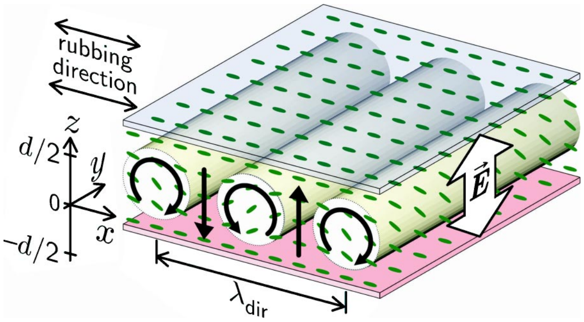

FIG. 1. (Color online) Sketch of the nematic cell with the director and flow fields in the electroconvection rolls and definition of the coordinate system.

at low excitation frequencies, the time-dependent amplitude $\varphi(t)$ of the director deflection preserves its sign, it is symmetric in the two halves of the excitation period, $\varphi(t)=\varphi(t+T/2)$. In the high-frequency, dielectric regime, on the other hand, $\varphi(t)$ is antisymmetric in time with respect to the two halves of the excitation period, $\varphi(t)=-\varphi(t+T/2)$. The cutoff frequency f_c separates the two dynamic regimes [7].

The consequence of these symmetries is that the Fourier transform of $\varphi(t)$ in the conduction regime contains only even multiples of the excitation frequency $f_0=1/T$, while in the dielectric regime, $\varphi(t)$ contains only odd multiples of f_0. In both regimes, the system response is T-periodic, i.e., the lowest frequency in the dynamics of the system variables is f_0.

It has been shown, however [27], that a certain class of wave forms, where $[E(t)\neq -E(t+T/2)]$, can evoke a subharmonic (T-antiperiodic) response of the pattern. The subharmonic regime has been identified in that previous study upon the application of two superimposed square waves with a frequency ratio 1:4, where one of the frequencies was chosen below the cutoff f_c for single-square-wave excitation, and the second frequency above f_c. The discovery of this interesting dynamic regime has motivated this study of the influence of the excitation wave form on the dynamic response of EHC patterns. We investigate the pattern dynamics at a particularly simple excitation scheme. dc-free triangular wave excitations (with frequency f_0 and amplitude E_0) are used as two-parameter functions, and the qualitative and quantitative influences on the pattern state diagram are studied.

The problem of subharmonic dynamics has been discussed for different types of dynamic systems in literature [31,32], and it has been shown that in a large class of systems, viz. periodic excitation with a wave form of the symmetry $E(t)=E(t+T)=-E(t+T/2)$, subharmonic dynamics is suppressed. We will refer to this type of function as antisymmetric excitation. Its Fourier expansion contains only odd numbered harmonics of the ground frequency $f_0=1/T$. We have therefore chosen an appropriate wave form, the triangular wave

$$E^{\mathrm{t}}(t)=\begin{cases}(4t/T)E_0 & \text{for} \quad 0\leqslant t<T/4\\ (2-4t/T)E_0 & \text{for} \quad T/4\leqslant t<3T/4\\ (4t/T-4)E_0 & \text{for} \quad 3T/4\leqslant t<T\\ E^{\mathrm{t}}(t \bmod T) & \text{elsewhere,}\end{cases} \tag{1}$$

as an example of an antisymmetric excitation with respect to a time shift $t\to t+T/2$. The Fourier expansion of this excitation gives the series

$$E^{\mathrm{t}}(t)=\frac{8}{\pi^2}E_0\left(\frac{1}{1^2}\sin\omega t-\frac{1}{3^2}\sin 3\omega t+\frac{1}{5^2}\sin 5\omega t\mp\cdots\right),$$

with $\omega=2\pi f_0$. As a “counterpole” of this antisymmetric wave form, we have chosen the function in Eq. (2), which will be referred to in the following as “sawtooth” function,

$$E^{\mathrm{s}}(t)=\begin{cases}(2t/T)E_0 & \text{for} \quad 0\leqslant t<T/2\\ (2t/T-2)E_0 & \text{for} \quad T/2\leqslant t<T\\ E^{\mathrm{s}}(t \bmod T) & \text{elsewhere.}\end{cases} \tag{2}$$

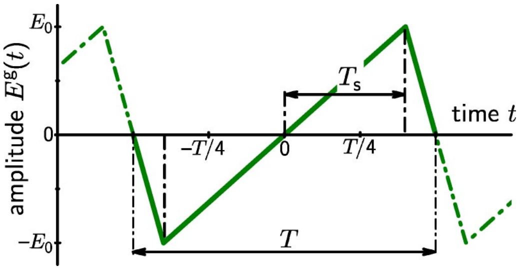

FIG. 2. General triangular excitation wave form. For $T_{\mathrm{s}}=T/4$ ($p=0$) one obtains the antisymmetric triangle of Eq. (1), and for $T_{\mathrm{s}}=T/2$ ($p=1$) the sawtooth function of Eq. (2).

The latter contains both even and odd numbered harmonics of the ground frequency $f_0=1/T$,

$$E^{\mathrm{s}}(t)=\frac{2}{\pi}E_0\left(\frac{1}{1}\sin\omega t-\frac{1}{2}\sin 2\omega t+\frac{1}{3}\sin 3\omega t\mp\cdots\right).$$

In addition, we will consider the general triangular wave form

$$E^{\mathrm{g}}(t)=\begin{cases}(t/T_{\mathrm{s}})E_0 & \text{for} \quad 0\leqslant t<T_{\mathrm{s}}\\ [(T/2-t)/(T/2-T_{\mathrm{s}})]E_0 & \text{for} \quad T_{\mathrm{s}}\leqslant t<T-T_{\mathrm{s}}\\ [(t-T)/T_{\mathrm{s}}]E_0 & \text{for} \quad T-T_{\mathrm{s}}\leqslant t<T\\ E^{\mathrm{g}}(t \bmod T) & \text{elsewhere,}\end{cases} \tag{3}$$

with $T/4\leqslant T_{\mathrm{s}}\leqslant T/2$. As a measure of the asymmetry of the excitation, we introduce the parameter $p=4T_{\mathrm{s}}/T-1$, which varies from $p=0$ for the triangular wave in Eq. (1) to $p=1$ for the sawtooth in Eq. (2). This general wave form allows us to study a gradual transition from the antisymmetric case of Eq. (1) toward the asymmetric sawtooth. Figure 2 visualizes the general excitation wave form given by Eq. (3).

We study a well-investigated standard liquid crystal mixture with known material parameters, where the experimental data can be directly compared to the theoretical results. The paper is organized in the following way: First, a description of the experimental conditions and the material is given. In the theoretical part of the paper, we analyze a system of model equations that describe the experiment. The dynamic response of the system variables is calculated. With a Floquet analysis we characterize the asymptotic stability of time-periodic solutions in the periodically driven dynamic system. The theoretical results are compared to experimental thresholds and wavelengths. In the third part, we investigate experimentally the detailed temporal characteristics of the patterns. We compare them to the calculated dynamics of the system.

II. EXPERIMENTAL TECHNIQUES AND MATERIAL

The material used, *Mischung 5*, is a nematic liquid crystal mixture of four alkyloxyphenylalkyl(oxy)benzoates. The dielectric anisotropy $\varepsilon_a = \varepsilon_\| - \varepsilon_\perp$ of this substance is negative, the conductivity anisotropy $\sigma_a = \sigma_\| - \sigma_\perp$ is positive. Its nematic range extends from 70.5 °C to below room temperature. The relevant material parameters that enter the model equations [33–35] are given in the Appendix .

The electrohydrodynamic convection patterns are investigated experimentally by using a commercial glass cell with a cell gap of $d = 48.5\ \mu$m. The two glass plates of the cell are coated with transparent indium-tin-oxide (ITO) layers serving as electrodes, with an electrode area of 5×5 mm^2. Rubbed polyimide layers orient the director planarly at the surfaces (see Fig. 1).

A Linkam heating stage provides a constant sample temperature of 30.0 ± 0.1 °C. Excitation voltages of different wave forms are synthesized with a function generator (Agilent 33220A), amplified and applied to the cell electrodes. Any dc offset is avoided.

For the spatiotemporal characterization of the experimental patterns, two optical observation techniques are used. In the transmission microscope, one has direct access to the spatial structure of the convection pattern. The texture reflects the momentary state of the deflected director field. This direct orthoscopic observation technique yields pattern wavelengths and orientations of the rolls, and in addition structures of defects and defect dynamics which are not relevant here. Its disadvantage is a large data overhead when one is interested only in the dynamics of pattern amplitudes. Another problem is the limited temporal resolution with conventional video technique, which is solved here by the use of a fast video camera (Citius Imaging C10). Experimental image sequences are recorded with a frame rate between 1000 and 2000 s^{-1}. The observation of optical textures is realized by a polarization microscope (Jenapol D) in an orthoscopic construction. It is used for a qualitative characterization of the dynamics. In the parallel polarizer-analyzer arrangement chosen for contrast optimization, only the extraordinary transmitted light is detected. As the effective refractive index of the birefringent nematic material for the normally incident light is a function of the director field deformation, the observed spatial intensity modulation of the transmitted light is a measure of the periodic director deflection amplitude. The time evolution of a cross section of the pattern, taken normal to the stripe direction, is extracted from the video [26,30]. The complete spatiotemporal behavior of the respective pattern can be reduced to a two-dimensional plot without loss of information under the condition that one has with normal rolls at onset, i.e., the patterns are uniform along the y direction, normal to the director easy axis. From these spatiotemporal data, a two-dimensional (2D) Fourier transform is performed, which yields a straightforward representation of the pattern in the wave-vector–frequency domain. Because of nonlinear optical characteristics, the observed texture depends crucially upon the choice of the microscope focus plane. Even if the director deflection along the easy director axis is harmonic, the optical intensity modulation is more complex. A large number of papers have been devoted to the understanding of the optical properties of EHC patterns, e.g., Refs. [33,36–42]. A discussion of the optical textures and their relations to the director field can be found, e.g., in Refs. [36–38].

A second setup is used to study laser diffraction patterns created by the roll textures; details of the experiment are given in Ref. [33]. The sample is irradiated with normally incident laser light of 632.8 nm wavelength, and the intensity at the second-order Fraunhofer diffraction peak is recorded by a photo diode. The relation between diffraction intensities and director deflection amplitudes is described., e.g., in Refs. [33,40–42]. This diffraction experiment has the advantage of a fast and quantitative access to the dynamics of the dominant Fourier mode of the director pattern. It is performed for a quantitative comparison of experimental trajectories with the dynamics calculated in the model.

III. MODEL

For the calculation of the onset of convection, we analyze the stability of the linearized electrohydrodynamic equations [7,12,35,43] with the spatial mode ansatz of the director deflection $\tilde{\varphi}(x,z,t)$ respective to the ground state. The linear stability analysis of the uniform ground state yields the instability thresholds, pattern wavelengths, and the pattern dynamics at onset.

The ground state is uniformly aligned along x, and within the two-dimensional model, homogeneity along y is assumed. The y component of the wave vector $\vec{k}$ of the roll pattern is set to zero (normal rolls). In our system, the experimental observations justify this assumption of $k_y = 0$ at onset, with the exception of very low frequencies where oblique rolls form the first instability. For the correct description of such oblique rolls with $k_y \neq 0$, the calculations would have to be refined correspondingly. For the electric charge field $\tilde{q}(x,z,t)$, an ansatz with the same spatial periodicity as the director field follows from the Maxwell equations:

$$\tilde{\varphi}(x,z,t) = \varphi(t)\cos(k_x x)\cos(k_z z),$$

$$\tilde{q}(x,z,t) = q(t)\sin(k_x x)\cos(k_z z). \tag{4}$$

Coordinates x,y are in the cell plane, z is along the cell normal (Fig. 1). The ansatz $k_z = \pi/d$ considers the ground mode that satisfies rigid planar anchoring conditions for the director at the polyimid coated glass plates, $\tilde{\varphi}(x, \pm d/2, t) = 0$. The wave number $k_x = 2\pi/\lambda_{\mathrm{dir}}$ reflects the spatial period λ_{dir} of the director pattern.

Using the Navier-Stokes equation, the Maxwell equations and the torque balance for the director one arrives at a system of nonlinear partial differential equations where the flow field in the nematic material can be eliminated (see, e.g., Ref. [12]). Free boundary conditions for the flow field have been used here. This approximation leads only to small quantitative differences in the predicted threshold voltages and corresponding wave numbers [9]. The linearization in the dynamic model reduces the system to a set of two coupled homogeneous ordinary differential equations for the two dynamic variables,

$$\frac{d}{dt}\vec{\xi}(t) + \mathbf{A}(t)\vec{\xi}(t) = 0, \tag{5}$$

$$\vec{\xi}(t)=\begin{pmatrix}q(t)\\ \varphi(t)\end{pmatrix}, \quad \mathbf{A}(t)=\begin{pmatrix}a_1 & a_2E(t)\\ a_3E(t) & a_4+a_5E(t)^2\end{pmatrix}, \tag{6}$$

where $E(t)$ is the electric field strength, related to the applied voltage by $E(t)=U(t)/d$, and the coefficients a_i depend upon the wave number k_x of the test mode and on material parameters; see the Appendix.

We sketch now in short the basis of the stability analysis, for details the reader is referred to standard literature, e.g., Ref. [44]). For systems of two and more coupled ODE's, an analytic solution in closed form exists only for a few special types of matrices $\mathbf{A}(t)$. For time-independent matrices $\mathbf{A}$, the ODE system (5) reduces to a system with constant coefficients with the formal solution $\vec{\xi}(t)=\mathbf{X}(t)\vec{\xi}(0)$, $\mathbf{X}(t)=\exp(-\mathbf{A}t)$. This can be exploited to compose analytical solutions for piecewise constant excitation wave forms. An application to the analytical treatment of EHC at square wave excitation is given in Ref. [27].

Equation (5) is equivalent to the matrix equation

$$\dot{\mathbf{X}}(t)+\mathbf{A}(t)\mathbf{X}(t)=0. \tag{7}$$

Using the fundamental matrix solution $\mathbf{X}(t)$ with the particular initial condition $\mathbf{X}(0)=\mathbf{E}$, the unit matrix, the solution of Eq. (5) is given by $\vec{\xi}(t)=\mathbf{X}(t)\vec{\xi}(0)$. For a time-periodic matrix $\mathbf{A}(t+T)=\mathbf{A}(t)$, describing an excitation $E(t)$ with period T, the Floquet theorem yields the particular form

$$\mathbf{X}(t)=\mathbf{Q}(t)e^{\mathbf{B}t}, \tag{8}$$

where both $\mathbf{Q}(t)=\mathbf{Q}(t+T)$ and $\mathbf{B}=\text{const}$ are 2×2 matrices, and consequently $\mathbf{X}(t+T)=\mathbf{X}(t)\mathbf{C}$, with the regular transfer matrix $\mathbf{C}=\mathbf{X}(T)=\exp(\mathbf{B}T)$ of the periodically excited system. The eigenvalues μ_i of $\mathbf{C}$ are called characteristic multipliers, and any λ_i such that $\mu_i=e^{\lambda_i T}$ is called characteristic exponent [44]. A necessary and sufficient condition for asymptotic stablility of periodic systems is that all $|\mu_i|<1$. We will choose $|\mu_1|\geqslant|\mu_2|$ in the following.

The determination of the coefficients and eigenvalues of $\mathbf{C}$ is as complex as the construction of the fundamental matrix solution $\mathbf{X}(t)$. We note that there is no simple relation between the elements of $\mathbf{A}(t)$ and the multipliers μ_i, but it is proven for homogeneous ODE systems like that given in Eq. (7) that $\det(\mathbf{C})=\mu_1\mu_2=\exp(-\int_0^T \mathrm{Tr}\,\mathbf{A}(t)dt)$ [44]. Since our $\mathbf{A}(t)$ has only real coefficients, this product is positive.

For all excitation wave forms considered here, we determine the elements and eigenvalues of $\mathbf{C}$ by straightforward numerical calculation of Eq. (7) over one period. At fixed T and given excitation wave form $E(t)$, the two parameters that have to be considered are the amplitude of the excitation, $U_0=E_0d$, and the wave number k_x of the test mode. The regions of instability of the ground state $\vec{\xi}_0=(0,0)$ in the (U_0,k_x) plane are defined by $|\mu_1|>1$ and bound by the neutral curve $\mathcal{N}$ where $|\mu_1|=1$. The global minimum of the neutral curve respective to U_0 defines the threshold voltage $U_c=E_cd$, with the corresponding critical wave number k_c. It is evident that solutions with $\mu_1=1$ reproduce the original state after one period of the excitation field, we will therefore refer to them as T-periodic solutions, the lowest frequency in their Fourier expansion (ground mode) is f_0. Solutions with $\mu_1=-1$ reproduce the original state only after two excitation periods, their Fourier expansion contains $f_0/2$ as the lowest frequency, and they will be therefore referred to as subharmonic or T-antiperiodic in the following. Regions with $\mu_1>1$ in the stability diagram correspond to growing T-periodic solutions, regions with $\mu_1<-1$ correspond to growing subharmonic solutions, for $|\mu_1|<1$, the ground state is asymptotically stable.

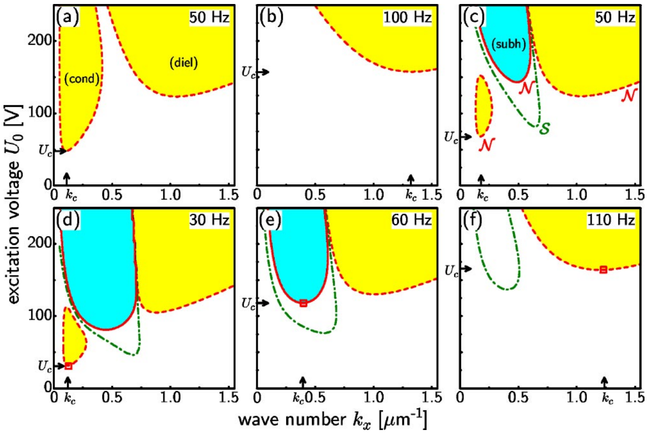

FIG. 3. (Color online) Representative calculated stability diagrams for EHC under different driving conditions, (a) triangular wave with $p=0$, $f<f_c$, (b) triangular wave with $p=0$, $f>f_c$, (c) general triangular wave with $p=0.6$, $f<f_c$, and (d)–(f) sawtooth excitation with $p=1$ at three selected excitation frequencies f_0, (d) conduction regime with lowest threshold, (e) subharmonic regime with lowest threshold, and (f) dielectric regime with lowest threshold. The excitation frequencies f_0 are given in the images. The neutral curve $\mathcal{N}$ is drawn as a dashed line at $\mu_1=1$, and as a solid line at $\mu_1=-1$. The dash-dotted line marks the separatrix $\mathcal{S}$ where $\mathrm{Re}\{\mu_{1,2}\}=0$. Colored areas represent regions where $|\mu_1|>1$, i.e., parameter regions where the ground state is unstable. Squares in (d)–(f) mark the three parameter sets where the trajectories of Figs. 6 and 12 have been evaluated.

Representative calculated stability diagrams are depicted in Fig. 3, where we have selected exemplarily the antisymmetric excitation ($p=0$), one wave form with the intermediate asymmetry parameter $p=0.6$ and the sawtooth excitation with $p=1.0$. Colored areas mark the parameter ranges where $|\mu_1|>1$, i.e., parameter ranges where the ground state is unstable with respect to convection patterns.

At antisymmetric triangular excitation ($p=0$) we find numerically that the multipliers $\mu_{1,2}$ are both real and positive for all parameter sets (U_0,k_x). The whole parameter space can be separated in two areas, one with conductivelike and the other with dielectriclike dynamics. In Fig. 3(a), which is representative for frequencies below the cutoff, there are two separate regions with $\mu_1>1$. The region at low k_x corresponds to patterns with the time symmetry of the conduction regime, the area at high k_x corresponds to dielectric patterns. The conduction regime provides the global minimum (arrows at U_c and k_c) of the neutral curve $\mathcal{N}$. In the experiment, when the amplitude U_0 of the driving voltage is gradually increased from zero, the pattern with the lowest threshold, i.e., the conduction pattern with wave number k_c, becomes unstable at $U_0 = U_c$. With increasing frequency, the instability island of the conduction patterns shifts to higher voltages in the (U_0, k_x) diagram. At f_c, it disappears completely or it has shifted such that the global minimum of $\mathcal{N}$ is found for the dielectric regime [Fig. 3(b)]. Although this reflects only the long established classical EHC behavior, and is qualitatively in complete coincidence with periodic sine or square wave driving, we present both graphs here in order to show the differences to the asymmetric wave forms presented in the next graphs.

In presence of asymmetric contributions $(p > 0)$ to the excitation, the topology of the stability diagram shows a dramatical qualitative change [Fig. 3(c)]. Already at very small values of p a subharmonic "island" appears between the conduction and dielectric regions. Within that island, both μ_i are negative. With increasing p, the parameter range covered by the subharmonic solutions spreads. It is separated from the classical regimes by a separatrix $\mathcal{S}$ (dash-dotted line) where $\text{Re}\{\mu_{1,2}\} = 0$ (the two multipliers are complex conjugated in a narrow parameter range around $\mathcal{S}$, otherwise real [45]). Further increase of p leads to the formation of an unstable subharmonic region with $\mu_1 < -1$ [dark (blue) area in Fig. 3(c)]. However, below a certain value of the asymmetry parameter $(p_c \approx 0.76)$ the global minimum of $\mathcal{N}$ remains in the conductive or dielectric branch for any excitation frequency. The uniform ground state becomes unstable with respect to one of the classical regimes first, a subharmonic pattern is not formed at onset. Whether the system could be forced into the subharmonic regime at higher voltages, under certain external obstructions, cannot be answered within our linear model.

The images of Figs. 3(d)–3(f) show the stability diagrams for excitation with the sawtooth $(p = 1)$. Here, the conduction regime exists for low frequencies, and it has the lowest threshold of the three instability islands. With increasing f_0, the region of conduction patterns shifts upward in the (U_0, k_x) and finally it disappears. At a first cutoff frequency f_{c1}, the subharmonic tongue extends below the conduction and dielectric regions in the (U_0, k_x) diagram. The subharmonic region provides the global minimum of $\mathcal{N}$ in a certain intermediate frequency range [Fig. 3(e)], and a pattern with subharmonic dynamics is observed in this range at onset. With further increasing frequency, the tip of the subharmonic tongue moves upwards to higher onset voltages. Above a second cutoff frequency f_{c2}, the subharmonic tongue has shifted above the dielectric range. Finally, the subharmonic island also disappears from the stability diagram. There may still exist a range where $0 > \mu_1 > -1$ in the diagram, but the dielectric regime with $\mu_1 > 1$ is the only remaining island of instability. Consequently, above f_{c2} the dielectric convection pattern is observed in the experiment.

After construction and evaluation of the stability diagrams for the complete frequency range under consideration, one can collect threshold voltages and critical wave numbers for given excitation wave forms, as is shown in Fig. 4. The antisymmetric triangular wave excitation yields the classical graphs shown in Fig. 4(a), with an increasing threshold voltage curve with frequency for the conduction roll pattern, and the transition to the dielectric regime at f_c. Furthermore, the wave numbers show slight slopes in both regimes and a discrete jump at f_c. A qualitatively similar pattern is obtained for slightly asymmetric wave forms [Eq. (3) with low p; a quantitative analysis is given below]. Figure 4(b) shows the same diagram for the sawtooth excitation with $p = 1$. Between the individual regimes, discrete wave number jumps are observed. Qualitatively similar diagrams are found for excitation with the general triangular wave form of Eq. (3) with sufficiently large p.

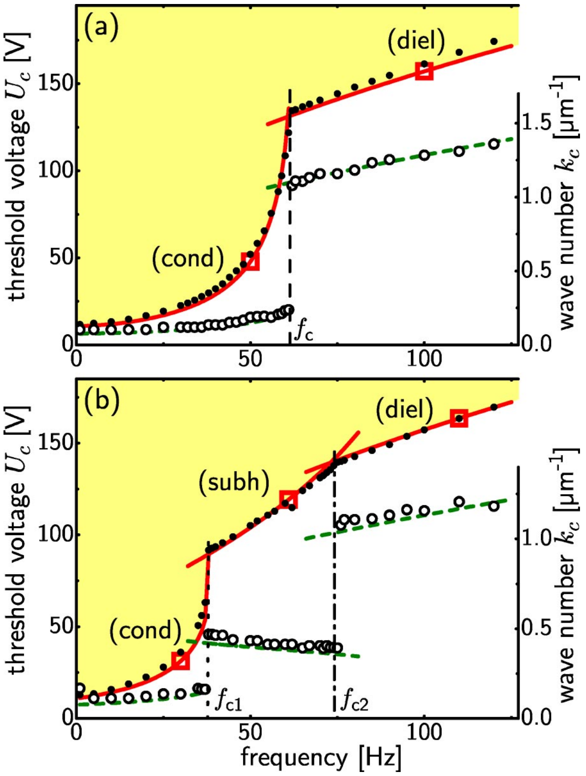

FIG. 4. (Color online) Calculated and measured threshold curves for (a) the antisymmetric triangular wave excitation, $p = 0$, and (b) the sawtooth excitation, $p = 1$. Solid lines give the calculated threshold voltages U_c for the pattern onset, dashed lines show the calculated critical wave numbers k_c at onset. The dots give the corresponding experimental threshold voltages, open circles give the wave numbers determined in the experiment (see next section). At $p = 0$, only the conductive and dielectric regimes are present, the cutoff frequency is $f_c = 60$ Hz. At $p = 1$, the subharmonic regime appears in a frequency range between $f_{c1} = 37$ Hz and $f_{c2} = 73$ Hz. The squares mark the parameters belonging to the corresponding graphs in Fig. 3.

There is a superficial analogy of the diagram in Fig. 4(b) with the graph presented in Ref. [27], where the threshold curve for superposition of two square waves has been determined in the same material. In Ref. [27], the two parameters were the amplitudes U_h, U_l of the two square waves with fixed frequencies and a 1:4 frequency ratio, where one of the frequencies had been chosen above, the second one below the cutoff frequency. In that situation, the compound wave form varied continuously along the threshold curve. Here, in contrast, the wave form is fixed, and the excitation frequency alone determines the transition between the different dynamic regimes.

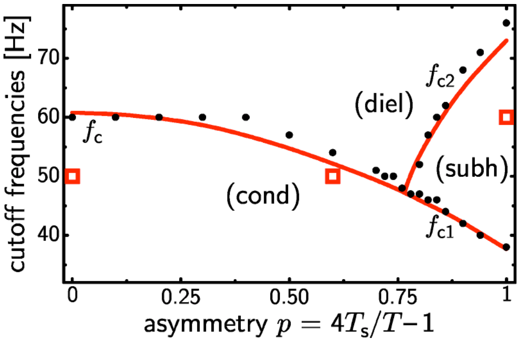

FIG. 5. (Color online) Transition frequencies between the conduction, dielectric, and subharmonic regimes in dependence of the asymmetry parameter p of the triangular wave form. The calculated (solid) lines mark the frequencies where the time symmetry of the pattern with the lowest threshold voltage changes. These frequencies correspond to f_c between (cond) and (diel), f_{c1} between (cond) and (subh), and f_{c2} between (subh) and (diel). Dots show the corresponding experimental data (see next section). The squares refer to the parameters of Figs. 3(a), 3(c), and 3(e). The subharmonic regime is found only at comparably large asymmetry parameters (above $p \approx 0.76$). Note that it is possible, according to this graph, to switch the pattern from a T-periodic to a T-antiperiodic time dependence only by a change of the wave form, when the ground frequency f_0 is kept constant.

An important question is the influence of the asymmetry of the excitation wave form on the appearance of the novel subharmonic regime. In order to investigate this wave form dependence in detail, pattern stability diagrams have been calculated for various asymmetry parameters p in the complete range $0 \leqslant p \leqslant 1$. From these graphs, we have constructed the dependence of the cutoff frequencies f_c, f_{c1}, and f_{c2} upon the asymmetry of the excitation wave form. The graphs are shown as solid lines in Fig. 5. It turns out that the cutoff frequency between the conduction and dielectric regimes is weakly dependent upon p for small asymmetries. There is a slight shift to lower frequencies, because the growing subharmonic tongue [cf. Fig. 3(c)] increasingly suppresses the conduction pattern instability island. Only at asymmetry parameters p above 0.76, the subharmonic regime appears in the threshold diagram and the single cutoff f_c splits into f_{c1} and f_{c2}. The remarkable result of this graph is that it is possible in this dynamic model system to pass from a T-periodic to a subharmonic response of the system at constant excitation frequency, only by a continuous change of the wave form, for example, when one varies the parameter p for the general triangular wave excitation, along any horizontal line with $37\ \mathrm{Hz} < f_0 < 73\ \mathrm{Hz}$. In addition, the transition between T-periodic and T-antiperiodic patterns can be achieved by a change of the excitation frequency at constant shape of the excitation wave form, e.g., by changing the frequency parameter along a vertical path in Fig. 5.

Finally, after establishing the general time symmetry of the pattern amplitudes, we discuss the numerically calculated trajectories of $\varphi(t)$ and $q(t)$ at onset during a cycle of the excitation. The asymptotic behavior is independent of the initial conditions, except for the degeneracy of solutions $\mathbf{(}\varphi(t), q(t)\mathbf{)} \leftrightarrow \mathbf{(}-\varphi(t), -q(t)\mathbf{)}$, cf. Eq. (5). In case of the antisymmetric triangle excitation ($p=0$), only the classical regimes appear at onset, with the T-periodic dynamics $q(t+T)=q(t)$, $\varphi(t+T)=\varphi(t)$ reflecting $\mu_1=1$. Additionally, one has the time symmetries $q(t+T/2)=-q(t)$, $\varphi(t+T/2)=\varphi(t)$ in the conduction regime and $q(t+T/2)=q(t)$, $\varphi(t+T/2)=-\varphi(t)$ in the dielectric regime. In case of any asymmetry of the excitation ($p>0$), the time symmetry respective to $T/2$ is broken in both regimes.

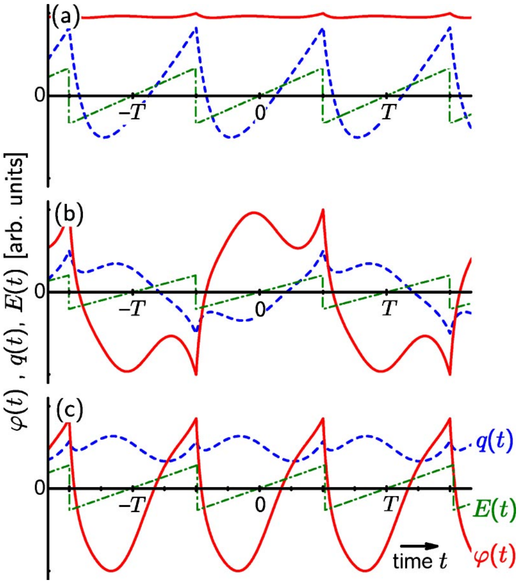

FIG. 6. (Color online) Calculated dynamics of the director deflection amplitude $\varphi(t)$ (solid line) and the charge field amplitude $q(t)$ (dashed line) for sawtooth excitation, $p=1$ (dashed-dotted line), with frequencies (a) 30 Hz, (b) 60 Hz, (c) 110 Hz. Note that the periodicity of $q(t)$ and $\varphi(t)$ is $2T$ in the subharmonic case (b). In the conduction (a) and dielectric (c) regimes, the signs of both $\varphi(t)$ and $q(t)$ are restored after one excitation period. Like for conventional sine or square waves, $\varphi(t)$ preserves its sign in the conduction regime (a) and alternates its sign twice during the excitation period in the dielectric regime (c). Squares in Fig. 3 mark the parameters U_0 and k_x where the trajectories (a)–(c) have been calculated.

In the case of the sawtooth wave form with $p=1$, the calculated dynamics is depicted in Figs. 6(a)–6(c). In contrast to the excitation with the antisymmetric triangle, sine, or square waves, both dynamic variables are no longer symmetric with respect to the half cycles of the driving field, $|\varphi(t)| \neq |\varphi(t+T/2)|$, $|q(t)| \neq |q(t+T/2)|$. The graphs show that in the conduction regime (a) as well as in the dielectric regime (c) both the director and charge fields are modulated with period T. The subharmonic regime is easily identified in the trajectories of Fig. 6(b). It is characterized by the fundamentally new symmetry $\varphi(t)=-\varphi(t+T)$, $q(t)=-q(t+T)$, where the amplitudes of both variables change their signs after one period T. This "antisymmetry" is a direct consequence of the sign of the Floquet multiplier $\mu_1=-1$.

IV. EXPERIMENTAL OBSERVATIONS

A. Fourier analysis of microscope textures

A direct evidence for subharmonic dynamics and the evaluation of the theoretical predictions on the basis of experimental data can be provided with an analysis of the optical microscope textures, which are sensitive to the sign of $\varphi(t)$. For that purpose, we record orthoscopic optical images of EHC patterns with sufficient time resolution.

In this section, we focus on two-dimensional Fourier transforms (2D FT's) of spatiotemporal plots of these experimental patterns. The method used here has been described in detail earlier [26]. The Fourier spectra are obtained by the following approach: The dynamic patterns are recorded with the high speed camera, the time resolution between individual frames was chosen between 0.5 and 1 ms. Then, a cross section along x (normal to the rolls) is selected. A spatiotemporal plot is constructed from the sequence of profiles along this section, extracted from a series of camera images; see, for example, Fig. 8(a). These plots are Fourier transformed digitally into the frequency-wave number domain, f represents the frequency axis, k is the wave number along the director easy axis x. For better clarity, the axes of all 2D FT spectra have been normalized with the director ground mode k_{dir} in the wave number domain and with the excitation frequency f_0 in the frequency domain. All images show the absolute value of the complex Fourier transform. The signal at $(f=0,\ k=0)$ corresponds to the integral optical intensity of the image. It does not contain information on the investigated patterns, therefore it has been set to zero in all Fourier transforms.

First, we recollect the classical time response of the director field. At pure sine or square wave excitation, the response of the director field is either strictly symmetric (conduction regime) or antisymmetric (dielectric regime) with respect to the two half periods of the driving field. Spatiotemporal patterns and their 2D FT spectra have been investigated in Ref. [26]. In the conduction regime, the pattern is nearly stationary at onset. The 2D FT yields the spatial ground mode k_{dir} and higher spatial harmonics at zero frequency. Spatial harmonics appear primarily because of the nonlinear relation between the optical transmission profile and the director deflection profile: even if the director deflection contains only the ground mode in x, the optical profile is not sinusoidal. In the dielectric regime, the amplitude $\varphi(t)$ of the spatial pattern is modulated with the excitation frequency, consequently one observes the dominating peak at the position (f_0, k_{dir}). Again, higher spatial harmonics reflect the optical nonlinearity of the texture. Because of the time symmetry $\varphi(t)=-\varphi(t+T/2)$, additional peaks appear only at odd harmonics $(2n+1)f_0$ of the excitation frequency. In particular, since the time integral of $\varphi(t)$ vanishes, there is no signal at the position $(0,\ k_{\mathrm{dir}})$ in a perfect pattern.

The situation for antisymmetric triangular wave excitation with $p=0$ [Eq. (1)] is qualitatively similar to sinus excitation. In the pattern state diagram shown in Fig. 4(a), experimental threshold fields and critical wave numbers are given as filled and open circles, respectively. Figures. 7 and 8 exemplarily show spatiotemporal patterns and 2D FT spectra in the two classical dynamic regimes. The texture in the conduction regime is a stationary stripe pattern along y, the corresponding spatiotemporal plot is a trivial array of stripes along the time axis, it has been omitted here. The spatiotemporal plot of the dielectric pattern near onset is shown in Fig. 8(a). The optical texture alternates synchronous to the electric field. After each half period, the pattern is shifted spatially by $\lambda_{\mathrm{dir}}/2$. This is a consequence of the symmetry $\tilde{\varphi}(x,z,t)=\tilde{\varphi}(x+\lambda_{\mathrm{dir}}/2,z,t+T/2)$.

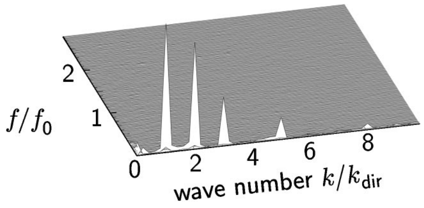

FIG. 7. 2D Fourier transform of an optical spatiotemporal pattern for antisymmetric triangular excitation in the conduction regime, $f_0=40$ Hz$<f_c$, $U_0=32.15$ V, $\lambda_{\mathrm{dir}}=30.2$ μm. The optical texture is a nearly stationary stripe pattern, the spatiotemporal pattern is not shown since it is trivial.

The 2D FT spectra are shown in Figs. 7 (conduction regime) and 8(b) (dielectric regime). In the conduction regime, one observes the peak of the stationary spatial ground mode and its higher spatial harmonics. Higher harmonics in the frequency domain are practically absent. The dielectric 2D FT pattern is dominated by the peak at (f_0, k_{dir}) and higher odd harmonics of f_0 in the time domain, an additional peak at $(3f_0, k_{\mathrm{dir}})$ is seen. The signal at $(0, k_{\mathrm{dir}})$ is practically absent because the time integral of $\varphi(t)$, vanishes.

In the case of the asymmetric sawtooth excitation with $p=1$, we find the pattern state diagram shown in Fig. 4(b) where open and solid circles represent the experimental data. The texture of conduction patterns is almost stationary, qualitative differences to antisymmetric excitation are practically not observable. These differences become evident only in a

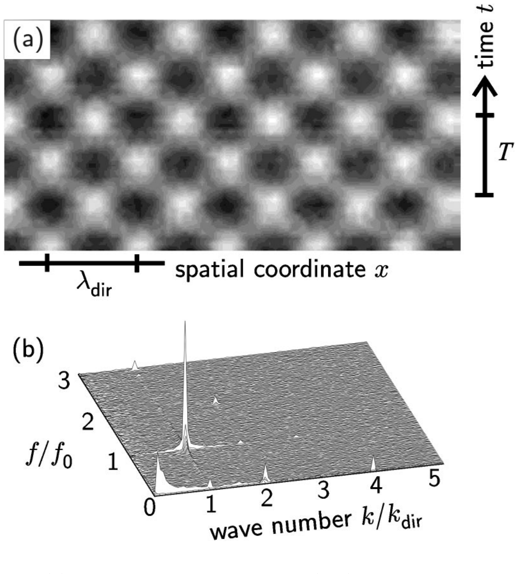

FIG. 8. (a) Spatiotemporal pattern $I(x,t)$ in the dielectric regime at triangular wave excitation [Eq. (1)], $f_0=65$ Hz$>f_c$, $U_0=139.3$ V. The spatial periodicity is $\lambda_{\mathrm{dir}}=5.7$ μm. In order to increase the signal-to-noise ratio, several images have been accumulated synchronously. Note that the time periodicity of the patterns is $T=1/f_0$ and there is a symmetry $I(x,t)=I(x+\lambda_{\mathrm{dir}}/2,t+T/2)$. (b) 2D Fourier transform of the spatiotemporal pattern shown in (a).

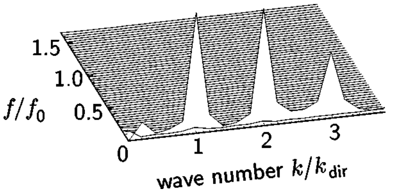

FIG. 9. 2D Fourier transform of an optical spatiotemporal pattern for simple sawtooth excitation in the conduction regime, $f_0 = 30\ \mathrm{Hz} < f_{c1}$, $U_0 = 34.35\ \mathrm{V}$, $\lambda_{\mathrm{dir}} = 29.7\ \mu\mathrm{m}$. The pattern is nearly time-constant, one observes only the stationary spectrum containing the director ground mode and higher spatial harmonics.

laser diffraction experiment which is much more sensitive to variations of $\varphi(t)$, cf. next section. However, the qualitative difference between asymmetric and antisymmetric excitation is obvious when one compares the spatiotemporal patterns in the dielectric regime; Figs. 8(a) and 10(a). The director responses have different time symmetries. A temporal shift of the spatiotemporal pattern by $T/2$ in time is no longer equivalent to any spatial shift of the pattern at sawtooth excitation. As is seen in Figs. 8(a) and 10(a), the spatial texture vanishes twice in each period of the driving field, i.e., the director deflection passes zero and changes its sign twice in each excitation period.

Figure 11(a) shows that in the subharmonic regime; the texture vanishes only once in each period of the driving field. This is agreement with the calculated trajectory of $\varphi(t)$ in Fig. 6, with only one sign change per period. In the spatiotemporal pattern, there is a symmetry $I(x,t) = I(x + \lambda_{\mathrm{dir}}/2, t+T)$, i.e., the pattern in subsequent cycles of the excitation field is spatially displaced by half a director period.

Figures 9 and 10(b), and 11(b) show the Fourier transforms of the optical patterns at sawtooth excitation. The pattern in the conduction regime is almost stationary in the vicinity of the threshold; higher harmonics in the frequency domain are at the limits of experimental resolution. In the dielectric regime, Fig. 10(b), one finds a dominating peak at (f_0, k_{dir}). This corresponds to an optical pattern with the periodicity of the director deflection, that alternates essentially with the excitation frequency. In contrast to antisymmetric excitation, additional peaks appear at even and odd harmonics of the excitation frequency. In particular, the peak at position $(0, k_{\mathrm{dir}})$ indicates that the time average of $\varphi(t)$ is in general not zero for asymmetric excitation. The pattern amplitudes in the two half periods of the excitation are not the same [Fig. 6(c)]. This has important consequences for the interpretation of conventional shadowgraph images of the convection patterns. Since the excitation frequencies are usually beyond the temporal resolution of the human observer or conventional video technique, only the time-averaged images are relevant there. The dielectric pattern at asymmetric excitation leaves a time-averaged image with the periodicity of the momentary images, while the spatial ground mode of the conventional, antisymmetrically driven dielectric patterns is averaged out. In that situation, one observes only an apparent texture that reflects the second spatial harmonics $(\lambda_{\mathrm{dir}}/2)$ of the director field.

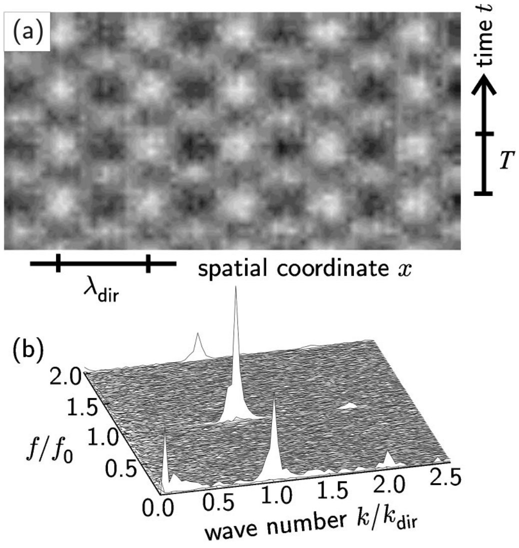

FIG. 10. (a) Spatiotemporal patterns in the dielectric regime at sawtooth excitation [Eq. (2)], $f_0 = 100\ \mathrm{Hz} > f_{c2}$, $U_0 = 162.95\ \mathrm{V}$, $\lambda_{\mathrm{dir}} = 5.5\ \mu\mathrm{m}$. In order to increase the signal-to-noise ratio, several images have been accumulated synchronously. Note that the period of the patterns is $T = 1/f_0$, but the symmetry $\varphi(t) = -\varphi(t+T/2)$ is broken. (b) 2D Fourier transform of the optical spatiotemporal pattern shown in (a). Peaks with wave number k_{dir} appear at $f=0$ and all harmonics of the excitation.

In the frequency range between f_{c1} and f_{c2} (subharmonic regime) in the pattern state diagram for sawtooth excitation [Fig. 4(b)], the Fourier spectra of the spatiotemporal patterns have the form shown in Fig. 11(b). The dominant peak is found at $(f_0/2, k_{\mathrm{dir}})$, i.e., the pattern is periodic with $2T$, and additional peaks of the spatial ground mode appear at frequencies $(2n+1)/2f_0$, $n = 1,2,3,\ldots$. We note that peaks belonging to k_{dir} and integer multiples of the excitation frequency are absent. In particular, the spectrum at f_0 is exactly

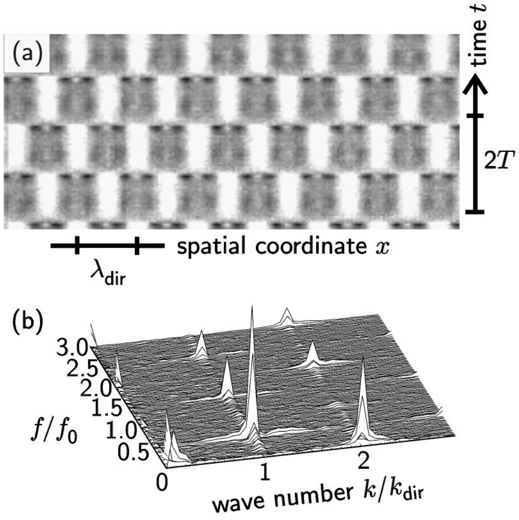

FIG. 11. (a) Spatiotemporal pattern at sawtooth excitation in the subharmonic regime, $f_{c1} < f_0 = 40\ \mathrm{Hz} < f_{c2}$, $U_0 = 96.9\ \mathrm{V}$, $\lambda_{\mathrm{dir}} = 9.6\ \mu\mathrm{m}$. (b) 2D Fourier transform of the optical spatiotemporal pattern shown in (a). Peaks appear at k_{dir} at $f = 0.5f_0, 1.5f_0, \ldots$.

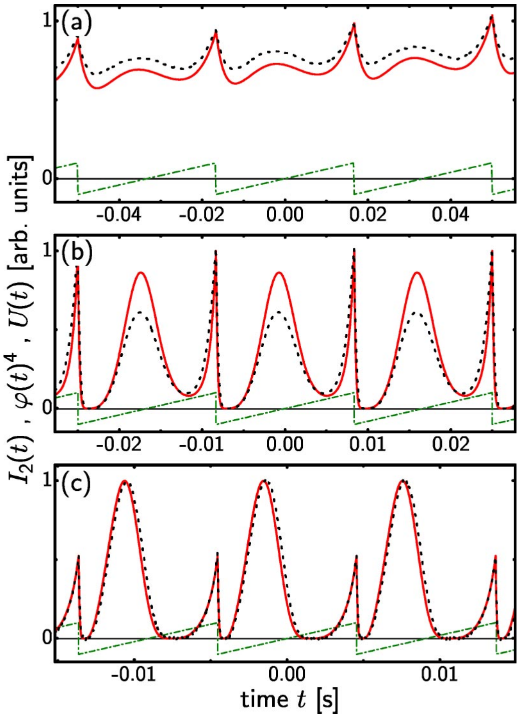

FIG. 12. (Color online) Measured intensities (dotted lines) of the second-order laser diffraction peak of the patterns in the (a) conduction, (b) subharmonic, and (c) dielectric regimes. The fourth power of the calculated director deflection amplitudes $\varphi(t)$ (Fig. 6), scaled to the same maxima as the experimental curves, are shown for comparison (solid lines). Except for slight quantitative deviations, the qualitative features of the trajectories are satisfactorily reproduced.

zero. This is a consequence of the time symmetry $\varphi(t+T) = -\varphi(t)$ of the convection pattern amplitude [cf. Fig. 6(b)]. The peaks at $2k_{\mathrm{dir}}$ and integer multiples of f_0 are, again, the consequence of the nonlinear relation between the optical contrast and the director deflection profile.

B. Laser diffraction experiments

Finally, we show that even the details of the system dynamics are qualitatively well reproduced by the model differential equation system. For that purpose, we have measured the time dependence of the diffraction profile generated by the modulated director field, with the setup described in Ref. [33]. The sample is irradiated with normally incident laser light, and the diffracted intensity at the second order peak is recorded by a photo diode. Figure 12 shows the time-dependent optical intensities for sawtooth excitation, $p = 1$, with exemplary excitation parameters in the conduction, subharmonic and dielectric regimes, respectively, (dotted lines). The corresponding parameter values are indicated by squares in Figs. 3(d)–3(f). Since the diffraction pattern is not sensitive to the sign of φ, the recorded signal in the subharmonic regime is of course equal in subsequent cycles of the excitation field.

For a comparison with the model, we take the calculated graphs $\varphi(t)$ of Fig. 6 and make use of the assumption that the second order diffraction peak intensity is proportional to $\varphi(t)^4$ [33]. The corresponding trajectories are depicted in Fig. 6 as solid lines. Since the linearized model can calculate the time dependence at threshold but not absolute values of the dynamic variables, the calculated curves have been scaled to the maxima of the experimental intensities. The details of the calculated time dependence of the system variables are in satisfactory agreement with the experiment.

V. SUMMARY

Summarizing, we have shown that time-asymmetric excitation $E(t) \neq -E(t+T/2)$ of electrohydrodynamic convection in nematics can generate a subharmonic dynamic response of the convection structure. By means of a spatiotemporal pattern analysis, on the basis of a 2D Fourier transform of the images, we have directly monitored the pattern dynamics. A continuous variation of the asymmetry of the excitation wave form has been investigated.

The analysis of the model equations shows that the island of subharmonic solutions in the stability diagram $\mu_1(U_0, k_x)$ is present already at very small deviations from a purely antisymmetric excitation $E(t) = -E(t+T/2)$. The range of existence of the subharmonic pattern increases continuously with the increasing asymmetry of the excitation wave form, represented by the shape parameter p. On the other hand, both experiment and theory show that the subharmonic pattern appears as the first instability only when the asymmetry parameter p has reached a value of approximately 0.76, i.e., when the wave form is already close to the sawtooth function of Eq. (2).

We have shown both in experiment and numerical model calculations that a transition from a T-periodic response to a T-antiperiodic, i.e., subharmonic, response of the investigated dynamic system can be achieved along two different routes. First, it occurs as an effect of increasing asymmetry of the wave form at constant frequency of the driving voltage. This is evident from Fig. 5, where a change of the wave form along a horizontal line in the phase space (at constant frequency) can bring the system from the dielectric or conduction regimes into the subharmonic regime and back. Second, it is evident from the same figure that for a constant wave form, e.g., the sawtooth excitation, the transition between these regimes can be achieved by a change of the frequency. This corresponds to the parameter change along a vertical line in Fig. 5 (const p). In a previous report, we have shown that other types of excitation wave forms may lead to subharmonic EHC patterns as well. A systematic investigation is under way to reveal global insight in the relation between the structure of the involved differential equation system, the excitation wave forms, and the dynamics of the system variables.

APPENDIX: COEFFICIENTS AND MATERIAL PARAMETERS

The coefficients in Eq. (6) in the cgs system are given by

$$a_1 = 4\pi \frac{\sigma_\parallel k_x^2 + \sigma_\perp k_z^2}{\varepsilon_\parallel k_x^2 + \varepsilon_\perp k_z^2}, \tag{A1}$$

$$a_2 = -\frac{(\sigma_\parallel \varepsilon_\perp - \varepsilon_\parallel \sigma_\perp)(k_x^2+k_z^2)}{\varepsilon_\parallel k_x^2 + \varepsilon_\perp k_z^2} k_x, \tag{A2}$$

$$a_3 = -\frac{1}{f}\left[\frac{1}{2}\frac{(\gamma_1-\gamma_2)k_x^4+(\gamma_1+\gamma_2)k_x^2k_z^2}{\alpha_1 k_x^2 k_z^2+(k_x^2+k_z^2)(\eta_1 k_x^2+\eta_2 k_z^2)} - \frac{\varepsilon_a k_x^2}{\varepsilon_\parallel k_x^2+\varepsilon_\perp k_z^2}\right]\frac{1}{k_x}, \tag{A3}$$

$$a_4 = \frac{K_{33}k_x^2 + K_{11}k_z^2}{f}, \tag{A4}$$

$$a_5 = \frac{1}{f}\left[\frac{-\varepsilon_a \varepsilon_\perp (k_x^2+k_z^2)}{4\pi(\varepsilon_\parallel k_x^2+\varepsilon_\perp k_z^2)}\right], \tag{A5}$$

with $k_z=\pi/d$, $\varepsilon_a=\varepsilon_\parallel-\varepsilon_\perp$ and the abbreviation

$$f = \gamma_1 - \frac{1}{4}\frac{[(\gamma_1-\gamma_2)k_x^2+(\gamma_1+\gamma_2)k_z^2]^2}{\alpha_1 k_x^2 k_z^2+(k_x^2+k_z^2)(\eta_1 k_x^2+\eta_2 k_z^2)}; \tag{A6}$$

see also Ref. [35]. Most of the material parameters are known from previous, independent experiments. The conductivities $(\sigma_\parallel, \sigma_\perp)$ are sensitively influenced by impurities in the material, their absolute values vary between individual cells. Therefore we fit these parameters for each individual cell by comparing calculated threshold voltages and wave numbers to measured data at simple triangle excitation. In detail, all calculations have been performed using the parameter set (in cgs units) $\varepsilon_\parallel=5.6$, $\varepsilon_\perp=6.0$, $\sigma_\parallel=96\ \mathrm{s}^{-1}$, $\sigma_\parallel/\sigma_\perp=1.5$, $\alpha_1=0.2\ \mathrm{g\ cm^{-1}\ s^{-1}}$, $\gamma_1=-\gamma_2=3.65\ \mathrm{g\ cm^{-1}\ s^{-1}}$, $\eta_1=4\ \mathrm{g\ cm^{-1}\ s^{-1}}$, $\eta_2=0.4\ \mathrm{g\ cm^{-1}\ s^{-1}}$, $K_{11}=14.9\times10^{-7}\ \mathrm{g\ cm\ s^{-2}}$, $K_{33}=13.76\times10^{-7}\ \mathrm{g\ cm\ s^{-2}}$.

[1] R. Williams, J. Chem. Phys. **39**, 384 (1963).

[2] A. P. Kapustin and L. K. Vistin, Kristallografiya **10**, 118 (1965).

[3] E. F. Carr, J. Chem. Phys. **38**, 1536 (1963).

[4] W. Helfrich, J. Chem. Phys. **51**, 4092 (1969).

[5] I. W. Smith *et al.*, J. Phys. Colloq. **C1**, 237 (1975).

[6] E. Dubois-Violette, P. G. de Gennes, and O. Parodi, J. Phys. (Paris) **32**, 305 (1971).

[7] L. Kramer and W. Pesch, Annu. Rev. Fluid Mech. **27**, 515 (1995).

[8] W. Zimmermann and L. Kramer, Phys. Rev. Lett. **55**, 402 (1985).

[9] E. Bodenschatz, W. Zimmermann, and L. Kramer, J. Phys. (Paris) **49**, 1875 (1988).

[10] M. Treiber and L. Kramer, Phys. Rev. E **58**, 1973 (1998).

[11] L. Kramer, B. Dressel, H. Zhao, and W. Pesch, Mol. Cryst. Liq. Cryst. Sci. Technol., Sect. A, **364**, 101 (2001).

[12] L. Kramer and W. Pesch, *Pattern Formation in Liquid Crystals* (Springer, New York, 1995).

[13] A. Buka *et al.*, Phys. Rev. E **66**, 051713 (2002).

[14] M. Dennin, G. Ahlers, and D. S. Cannell, Phys. Rev. Lett. **77**, 2475 (1996); Science **272**, 388 (1996).

[15] H. Riecke and G. D. Granzow, Phys. Rev. Lett. **81**, 333 (1998).

[16] P. Toth *et al.*, Europhys. Lett. **57**, 824 (2002).

[17] U. Bisang and G. Ahlers, Phys. Rev. Lett. **80**, 3061 (1998).

[18] U. Bisang and G. Ahlers, Phys. Rev. E **60**, 3910 (1999).

[19] Y. Hidaka *et al.*, J. Phys. Soc. Jpn. **66**, 3329 (1997).

[20] K. Tamura, Y. Hidaka, Y. Yusuf, and S. Kai, Physica A **306**, 157 (2002).

[21] A. Buka, P. Toth, N. Eber, and L. Kramer, Phys. Rep. **337**, 157 (2000).

[22] J. H. Huh and S. Kai, Phys. Rev. E **68**, 042702 (2003).

[23] T. Peacock and T. Mullin, J. Fluid Mech. **432**, 369 (2001).

[24] S. Kai, S. Wakabayashi, and M. Imasaki, Phys. Rev. A **33**, 2612 (1986).

[25] U. Schneider, M. de la Torre Juarez, W. Zimmermann, and I. Rehberg, Phys. Rev. A **46**, 1009 (1992).

[26] H. Amm, M. Grigutsch, and R. Stannarius, Z. Naturforsch., A: Phys. Sci. **53a**, 117 (1998).

[27] T. John and R. Stannarius, Phys. Rev. E **70**, 025202(R) (2004).

[28] C. W. Meyer, D. S. Cannell, G. Ahlers, J. B. Swift, and P. C. Hohenberg, Phys. Rev. Lett. **61**, 947 (1988).

[29] H. Riecke, J. D. Crawford, E. Knobloch Phys. Rev. Lett. **61**, 1942 (1988); D. Walgraef, Europhys. Lett. **7**, 485 (1988).

[30] I. Rehberg, S. Rasenat, J. Fineberg, M. de la Torre Juarez, and V. Steinberg, Phys. Rev. Lett. **61**, 2449 (1988).

[31] J. W. Swift and K. Wiesenfeld, Phys. Rev. Lett. **52**, 705 (1984).

[32] T. P. Schulze, Phys. Fluids **11**, 3573 (1999).

[33] T. John, U. Behn, and R. Stannarius, Eur. Phys. J. B **35**, 267 (2003).

[34] T. John, U. Behn, and R. Stannarius, Phys. Rev. E **65**, 046229 (2002).

[35] U. Behn, A. Lange, and T. John, Phys. Rev. E **58**, 2047 (1998).

[36] S. Rasenat, G. Hartung, B. L. Winkler, and I. Rehberg, Exp. Fluids **7**, 412 (1989).

[37] A. Joets and R. Ribotta, Opt. Commun. **107**, 200 (1994).

[38] A. Joets and R. Ribotta, J. Phys. I **4**, 1013 (1994).

[39] S. P. Trainoff and D. S. Cannell, Phys. Fluids **14**, 1340 (2002).

[40] J. A. Kosmopoulos and H. M. Zenginoglou, Appl. Opt. **26**, 1714 (1987).

[41] T. O. Carroll, J. Appl. Phys. **43**, 767 (1972).

[42] M. Bouvier and T. Scharf, Opt. Eng. (Bellingham) **39**, 2129 (2000).

[43] P. Penz and G. Ford, Phys. Rev. A **6**, 414 (1972).

[44] J. Hale, *Ordinary Differential Equations*, 2nd ed. (Krieger, Malabar, FL, 1980).

[45] In that small region around $\mathcal{S}$, neither T-periodic nor T-antiperiodic (subharmonic) solutions of the differential equation system exist. We have to correct in that respect a statement in the caption of Fig. 7 in Ref. [27]; a detailed discussion will be given elsewhere.